Dimethylammonium copper formate [(CH_{3})_{2}NH_{2}]Cu(HCOO)_{3}: A metal-organic framework with quasi-one-dimensional antiferromagnetism and magnetostriction

Zhenxing Wang, Prashant Jain, Kwang-Yong Choi, Johan van Tol, Anthony K. Cheetham, Harold W. Kroto, Hyun-Joo Koo, Haidong Zhou, Jungmin Hwang, Eun Sang Choi, Myung-Hwan Whangbo, and Naresh S. Dalal

Phys. Rev. B **87**, 224406 — Published 10 June 2013

DOI: 10.1103/PhysRevB.87.224406

Dimethylammonium Copper Formate $[(CH_3)_2NH_2]Cu(HCOO)_3$: A Metal-organic Framework (MOF) With Quasi-One-Dimensional Antiferromagnetism and Magnetostriction

Zhenxing Wang[1,2], Prashant Jain[3*], Kwang-Yong Choi[4], Johan van Tol[1,2], Anthony K. Cheetham[5], Harold W. Kroto[1], Hyun-Joo Koo[6], Haidong Zhou[2], Jungmin Hwang[2,7], Eun Sang Choi[2], Myung-Hwan Whangbo[8] and Naresh S. Dalal[1,2*]

[1] Department of Chemistry and Biochemistry, Florida State University, Tallahassee, FL 32306, USA

[2] National High Magnetic Field Laboratory, Florida State University, Tallahassee, FL 32310, USA

[3] LANSCE-LC & NHMFL-PFF, Los Alamos National Laboratory, Los Alamos, NM, 87544, USA

[4] Department of Physics, Chung-Ang University, 221 Huksuk-Dong, Dongjak-Gu, Seoul 156-756, Republic of Korea

[5] Department of Materials Science and Metallurgy, University of Cambridge, Cambridge CB2 3QZ, UK

[6] Department of Chemistry and Research Institute for Basic Sciences, Kyung Hee University, Seoul 130-701, Republic of Korea

[7] Department of Physics, Florida State University, Tallahassee, FL 32306, USA

[8] Department of Chemistry, North Carolina State University, Raleigh, NC 27695, USA

Corresponding Authors: dalal@chem.fsu.edu (N. S. Dalal)

prashant@lanl.gov (P. Jain)

Abstract

Metal-organic frameworks (MOFs) exhibit many interesting properties such as multiferroic behavior, dipolar glass, gas storage, and protonic conductivity. Here we report that dimethylammonium copper formate (DMACuF) $[(CH_3)_2NH_2]Cu(HCOO)_3$, a cation templated non-porous MOF with perovskite topology, exhibits strong one-dimensional (1D) antiferromagnetism with a Néel temperature, T_N, of 5.2 K. These conclusions are derived from detailed magnetic susceptibility, heat capacity, dielectric constant, and high frequency electron paramagnetic resonance (HF-EPR) measurements as well as density functional theory (DFT) calculations. The magnetic susceptibility exhibits a broad maximum at ~50 K, suggesting low-dimensional magnetism; heat capacity measurements showing a Néel temperature of 5.2 K. The magnetization versus field data at 1.8 K shows a spin-flop transition at H_{sf}~1.7 T. The ratio $T_N/J = 6.5 \times 10^{-2}$, where J is the near-neighbor exchange constant (77.4 K), and the small value (2 K) of the inter-chain coupling suggests that DMACuF is close to an ideal 1D magnet. In this 3-D crystal lattice, the 1-D magnetic behavior is made possible by the Jahn-Teller distortion of the $3d^9$ Cu^{2+} ions. Temperature dependence of the EPR resonance field and the linewidth exhibits critical broadening for temperatures below 50 K, following a behavior quite characteristic of 1D spin systems. DFT calculations show that $[(CH_3)_2NH_2]Cu(HCOO)_3$ has a magnetic structure in which 1D antiferromagnetic chains parallel to the c-direction are weakly coupled ferromagnetically, supporting the thermomagnetic and EPR results. Dielectric measurements under applied magnetic fields of 0–7 T reveal a kink at the T_N, a clear indication of magnetostriction behavior, a first for these MOFs.

1. Introduction

In recent years MOFs have received a great deal of attention because they have not only useful applications in catalysis and gas storage but also possess novel optical and dielectric properties.[1-10] The formate ion $HCOO^-$, the smallest carboxylate, has been widely used to bridge two or more transition-metal ions and forming zero-, one-, two- and three dimensional (0D, 1D, 2D and 3D, respectively) complexes.[11] Recently, multiferroic properties were found for those

MOFs with ABX_3 perovskite architecture, $[(CH_3)_2NH_2]M(HCOO)_3$ (DMAMF = dimethylammonium metal formate), where M = Mn, Co, Ni, and Fe.[8, 11-13] These studies present a new approach to synthesizing multiferroic materials.

Regarding the dielectric properties of these DMAMFs, Jain *et al*.[8] have shown that DMAMnF, DMACoF and DMANiF undergo paraelectric to ferroelectric phase transitions at 160, 165, and 180 K, respectively. Their dielectric constants for the paraelectric phases are approximately 45, 50, and 30, respectively. Powder X-ray diffraction (PXED) data showed that a significant lattice contraction took place on cooling when passing the transition temperatures. The main peaks in the PXRD pattern also showed splitting, which is associated with symmetry lowering. Jain *et al*. also performed heat capacity measurements on DMAMnF over the temperature range of 1.8–300 K to observe an ordering at ~183 K with entropy change ΔS = 0.9 J/mol·K, which is significantly smaller compared with 9.1 J/mol·K expected for a simple 3-fold order-disorder model. DMAMnF thus becomes only partially ordered when cooled through the transition and the long-range ordering takes place over a broad range of temperatures.[9] Sánchez-Andújar *et al*.[13] further found that it changes the structure from $R\bar{3}c$ space group at room temperature to *Cc* at 100 K.

Concerning the magnetic properties, Wang *et al*.[11, 12] have reported that DMAMnF, DMACoF and DMANiF are weak ferromagnets with the critical temperature T_C = 8.5, 14.9, and 35.6 K, respectively. Their ferromagnetic spin exchange parameters between adjacent magnetic ions through the intervening $HCOO^-$ bridge are reported to be −0.46, −3.31, and −6.97 K, respectively. (Here we use the convention in which the ferromagnetic and antiferromagnetic spin exchanges are represented by negative and positive numbers, respectively). The heat capacity study of DMAMnF[8] indicates that the weak ferromagnetism originates from a canted antiferromagnetic ordering at T_N = 8.4 K under zero magnetic field. Detailed studies show that the T_N decreases from 8.4 to 6.7 K with increasing magnetic field from 0 to 9 T. Subsequent Q-band (35 GHz) EPR measurements also confirmed the ordering in DMAMnF at ~6 K.

Dimethylammonium copper formate (DMACuF) was first reported by Sletten and Jensen[14] and has been studied by muon spin relaxation measurements.[15] It crystallizes in a monoclinic space group of *C2/c* and has a distorted ReO_3-like structure as depicted in Fig. 1a. Each Cu^{2+} ion

forms an axially-elongated CuO_6 octahedron with six different $HCOO^-$ ions, each $HCOO^-$ ion bridging two adjacent CuO_6 octahedra so that the CuO_6 octahedra have a perovskite-like arrangement with the center of every Cu_8 cube occupied by a DMA cation. We realized that this compound might exhibit a 1- or 2-D magnetism, which would be novel in this class of MOFs. This notion derives from the fact that the magnetic orbital ($d_{x^2-y^2}$ orbital) of the copper ion in each CuO_6 octahedron is contained in the CuO_4 square plane made up of four short Cu-O bonds (Fig. 1b). For convenience, the short and long Cu-O bonds will be referred to as the Cu-O_{eq} and Cu-O_{ax}, respectively. The interactions of the CuO_6 units are illustrated in Fig. 1c. Cu-O…O-Cu spin exchange interaction can be substantial only when both Cu-O bonds are Cu-O_{eq} bonds (J_1). Importantly, the interactions between these chains (J_2 and J_3) are weak because they are described by the Cu-O_{eq}…O_{ax}-Cu spin exchanges.[16-18] Therefore, DMACuF is expected to exhibit a 1D magnetic character to a first approximation. In the present work we characterize the magnetic properties of DMACuF by magnetic susceptibility, heat capacity, high frequency electron paramagnetic resonance (HF-EPR), and dielectric constant measurements. The experimental data are fully supported by density functional theory (DFT) calculations. A sharp kink is observed in the capacitance data at the T_N, showing that the compound exhibits magnetostriction, a first for this class of MOFs.

2. Experimental Details

The DC magnetic susceptibility of a single crystal of DMACuF was measured using a Quantum Design MPMS SQUID magnetometer at 0.5 T between 1.8–300 K for both field-cooled (FC) and zero-field-cooled (ZFC) modes. Its magnetization was measured at 1.8 K at fields up to 7 T with the field applied along the g_z-axis (see Fig. 6(a) for a sample orientation). The heat capacity, C_P, of a polycrystalline sample was measured using a Quantum Design PPMS (Physical Property Measurement System) over 1.8–200 K by employing the heat pulse-relaxation method as described earlier.[8] Powder and single crystal samples were used in the HF-EPR measurements. 5 mg crystals were grinded, mixed with 100 mg KBr, and pressed into a pellet for the powder EPR measurements. The temperature and angular dependence at 240 GHz were

measured using a super-heterodyne cw/Pulsed EPR spectrometer, equipped with a rotator stage.[19, 20] Dielectric constant measurements were made by measuring capacitance of a pelleted sample with parallel capacitor geometry, as described previously.[21]

The DFT calculations employed the projector augmented wave (PAW) method encoded in the Vienna ab initio simulation package (VASP),[22-24] and the generalized-gradient approximation (GGA) of Perdew, Burke and Ernzerhof[25] for the exchange-correlation functional with the plane-wave-cut-off energy of 400 eV and a set of 6×6×4 k-points to cover the irreducible Brillouin zone. To examine the effect of electron correlation associated with the Cu 3d states, the GGA plus on-site repulsion method (GGA+U)[26] was used with the effective U_{eff} values of 4–7 eV.

3. Results

3.1 Magnetic Susceptibility and Magnetization

Figure 2 shows the temperature dependence of the magnetic susceptibility $\chi(T) = M(T)/H$ obtained from a single crystal of DMACuF with the external field of $B = 0.5$ T applied along the g_z-axis. The ZFC and FC data display essentially the same behavior. With decreasing temperature the magnetic susceptibility shows a broad maximum around $T_{max} = 51$ K, and then a rapid drop at about 6.8 K. The former is characteristic of an $S = -1/2$ 1D Heisenberg antiferromagnet while the latter is expected for ordered collinear antiferromagnets. At the lowest measured temperature (1.8 K), the susceptibility still has an appreciable residual value, which suggests that the measured g_z-axis lies between the easy and hard axes. In the high-temperature regime ($T > 80$ K) the susceptibility is well described by the Curie-Weiss law $\chi(T) = C/(T - \theta)$ with the Curie-Weiss temperature $\theta = -80.6$ K, which indicates the presence of dominant antiferromagnetic spin exchange interactions between the Cu^{2+} ($S = 1/2$) ions.

Figure 3 shows the magnetization curve versus external field measured at 1.8 K. The external field is applied parallel to the g_z-axis as in the magnetic susceptibility. The magnetization curve exhibits a rather steep increase up to 3 T and then a quasi-linear dependence. Since a heat capacity and a dielectric constant show no magnetic and lattice anomalies in the respective field range, this increase is ascribed to the spin-flop transition which is the hallmark of

an antiferromagnet when an external field is applied along an easy axis.[27] We identify the spin-flop transition field as H_{sf}~ 1.7 T by taking a derivative of the measured magnetization with respect to field (see the inset of Fig. 3). In our case, the transition is smooth rather than abrupt. This is due to the fact that the measured g_z-axis is not an easy axis but it is close to an intermediate axis. In addition, low-dimensional quantum fluctuations smooth-out the expected first-order transition. In turn, a further study of the temperature and angular dependence is beyond the scope of the present work, but could be very rewarding.

3.2 Heat capacity

The temperature dependence of the heat capacity was measured to get further information about the long-range order. As shown in Fig. 4A, a clear peak was observed around 5.2 K in the Cp/T^2 vs T plot, together with a linear behavior below this temperature. These are typical for a transition to an antiferromagnetically ordered state.[28] In addition, for a Heisenberg antiferromagnetic 1D chain, we expect the maximum of the magnetic heat capacity at $0.48J \approx 38$ K.[29] This provides another way of determining the strength of the leading magnetic interactions. However, the experimental curve has no discernible feature in the vicinity of 38 K due probably to the dominance of the phonon contribution to the heat capacity. Since an isostructural non-magnetic reference compound is not available, the separation of the magnetic contribution is not possible.

We turn to the field dependence of the heat capacity. As shown in Fig. 4B, applying a magnetic field leads to an increase of the size of the anomaly as well as to a slight shift of the transition temperature to higher temperatures, from $T_N = 5.32$ K at $B = 0$ T to $T_N = 5.46$ K at $B = 9$ T. This is contrasted by a mean-field behavior, yielding the reduction of T_N. Since the Cu^{2+} ion has negligible single-ion anisotropies, it should be ascribed to enhanced low-dimensional quantum fluctuations.

3.3 Electron Paramagnetic Resonance

In order to study the critical spin dynamics of the 1D spin chains, we performed HFEPR measurements on powder as well as single crystals of DMACuF. Figure 5 shows an EPR

spectrum of a powder at 108 GHz and 150 K. The spectrum is composed of three peaks, which could be well simulated[30] with three effective *g*-values for an $S = 1/2$ powder, $g_x = 2.0731$, $g_y = 2.1756$ and $g_z = 2.2759$.

To determine the directions and magnitudes of the *g*-tensor components in crystals to assist further studies, we measured EPR spectra with a single crystal oriented in different planes. Fig. 6A shows the angular dependence of the effective *g*-values (resonance field) as a function of the angle θ for three orthogonal planes at 300 K. As can be seen, the effective *g*-values shift between two of the three *g*-values obtained in Fig. 5. By doing the angle dependence, we are able to find out the *g*-vectors in a single crystal (inset of Fig. 6A) so that the crystal can be aligned well in other measurements. No particular feature related to 1D correlated systems was observed in these measurements, which could be due to the fact the 1D chain dynamics dies out when $T >> J$.

In order to study the spin dynamics, EPR measurements were performed on a single crystal at different orientations. Figures 7A and 7A' show the EPR spectrum as a function of temperature measured at 240 GHz for $B \parallel g_z$-axis and $B \parallel g_x$ axis, respectively. In both measurements, intriguing changes are shown with lowering temperature: strong broadening, shifting and then narrowing of the EPR peak.

3.4 Dielectric anomalies

DMAMFs show a transition to a ferroelectric phase. This motivated us to probe the coupling between magnetic order and dielectric properties. Figure 8 displays the temperature dependence of the dielectric constant measured for a powder sample. With decreasing temperature the dielectric constant exhibits a broad minimum around 17 K and upon further cooling, ε' shows a kink-like anomaly at the magnetic ordering temperature T_N. We observe no appreciable field dependence of ε' by applying an external field up to 7 T.

4. Discussions and Theoretical Evaluation

4.1 Magnetic Susceptibility and Magnetization

As shown in Sec. 3.1, the magnetic interactions of DMACuF are expected to be described by a uniform 1D Heisenberg antiferromagnet. Thus, we fitted the magnetic susceptibility data using

a Bonner-Fisher formula: [31]

$$\chi(T) = \frac{Ng^2\mu_B^2}{k_B T}\left[\frac{A_0 + A_1 X^{-1} + A_2 X^{-2}}{1 + B_1 X^{-1} + B_2 X^{-2} + B_3 X^{-3}}\right] \quad (1)$$

where g = 2.15 and $X = 2k_BT/J$ with J as the antiferromagnetic exchange coupling constant defining the spin Hamiltonian $\hat{H} = J\sum_i S_i S_{i+1}$ for a 1D spin chain. The magnetic susceptibility is well fitted by J = 77.4 ± 0.3 K in the whole temperature range down to the ordering temperature. The ratio of the Néel temperature to the nearest neighbor exchange, $T_N/J \approx 6.5 \times 10^{-2}$, is very small value, suggesting that the DMACuF is close to an ideal 1D magnet.

For a 1D Heisenberg antiferromagnet, the temperature of the maximum T_{max} and the height of the maximum χ_{max} are related to J as $T_{max} = 0.641J/k_B$ and $\chi_{max} = 0.147 \cdot Ng^2\mu^2_B/J$.[29] This relation gives J = 79.56 K, which is very close to the value obtained from the fitting. In addition, we can estimate the strength of the inter-chain coupling J_{inter} in the mean-field approximation as $|J_{inter}| = T_N / 1.28\sqrt{\ln(5.8J/T_N)} \approx 2$ K.[32] The small ratio $|J_{inter}|/J \approx 2.5 \times 10^{-2}$ provides additional evidence that the DMACuF realizes a nearly ideal Heisenberg antiferromagnetic 1D chain system. The sign of J_{inter}, not determined by the mean-field approximation,[32] is discussed further in Section 4.2.

4.2 Theoretical Calculations of the Spin Exchange Interactions

For the spin exchange interactions of DMACuF, we consider the intra-chain spin exchange paths J_1 as well as the nearest-neighbor inter-chain spin exchange paths, J_2 and J_3, shown in Figs. 1c and 1d. To evaluate the spin exchange parameters, $J_1 - J_3$, we determine the relative energies of the four ordered spin states in Fig. 9 on the basis of GGA+U calculations with U_{eff} = 4, 5, 6, and 7 eV. The relative energies of these spin states obtained from GGA+U calculations are summarized in Fig. 9. In terms of the spin Hamiltonian, the total spin exchange energies of these states are expressed as[16, 33, 34]

$E_{FM} = -(-4J_1 - 8J_2 - 8J_3)(N^2/4)$

$E_{AF1} = -(4J_1 - 8J_2 + 8J_3)(N^2/4)$

$E_{AF2} = -(-4J_1 + 8J_2 + 8J_3)(N^2/4)$

$E_{AF3} = -(4J_1 + 8J_2 - 8J_3)(N^2/4)$ (2)

by using the energy expressions obtained for spin dimers with N unpaired spin per spin site (in the present case, N = 1). Thus, by mapping the relative energies of the four ordered spin states onto the corresponding energies expected from the total spin exchange energies, we obtain the values of $J_1 - J_3$ summarized in Table 1. J_1 and J_3 are antiferromagnetic while J_2 is ferromagnetic. J_1 is by far the strongest spin exchange, and the strengths of the spin exchanges decrease as $J_1 >> |J_2| > J_3$ for all employed U_{eff} values. The J_1 evaluated from GGA+U calculations is larger than the experimental value by a factor of approximately two. This is usual because DFT calculations are known to overestimate the spin exchange parameters approximately up to 4 times.

As expected, the Cu-O_{eq}…Cu-O_{eq} unit forms a 1D chain. These 1D AFM chains ($J_1 > 0$) are weakly coupled through the ferromagnetic J_2 and the antiferromagnetic J_3 so that there is no spin frustration between the adjacent 1D chains. Note that the effective inter-chain exchange is given by the sum $J_2 + J_3$ per magnetic ion Cu^{2+}. Since $J_2 + J_3$ is ferromagnetic (i.e., $J_2 + J_3 < 0$), the J_{inter} derived from the mean-field approximation (see Section 4.1) should be ferromagnetic ($J_{inter} < 0$). Consequently, the resulting 3D magnetic structure of DMACuF should have the A-type antiferromagnetic structure,[35] in which layers of ferromagnetically coupled Cu^{2+} ions perpendicular to chain are antiferromagnetically coupled along the c-direction. Therefore, the magnetic unit cell of the 3D ordered antiferromagnetic structure remains the same as the chemical unit cell (Fig. 9b). It is desirable to confirm this conclusion by neutron diffraction measurements.

4.3 Electron Paramagnetic Resonance

Due to the strong antiferromagnetic exchange coupling (J_1) between the Cu^{2+} centers in a 1D chain, those observed *g*-values in Fig. 5 are only effective parameters, rather than the real values of a single Cu^{2+} ion. It is shown in Figs. 1a and 1c that the CuO_6 octahedras have two elongated orientations with a torsion angle 2θ of 70.82° as shown in Fig. 10A. One can relate the principal *g*-vectors ($g_{\|}$ and $g_{\perp}$) of the Cu centers and the three observed ones as illustrated in Figs. 10B and 10C. The vectors can be related by following equations:

$$g_z^2 = g_{\|}^2 \cos^2\theta + g_{\perp}^2 \sin^2\theta \quad (3)$$

$$g_y^2 = g_{\parallel}^2 \sin^2\theta + g_{\perp}^2 \cos^2\theta \quad (4)$$

$$g_x = g_{\perp} \quad (5)$$

with $\theta = 35.41°$. By calculation, single ion principal *g*-values were obtained, $g_{\parallel} = 2.3784$ and $g_{\perp} = 2.0731$. In addition, we can also relate the directions of g-vectors with the unit cell edges (Fig. 6B).

To understand strong temperature dependence of EPR spectra shown in Fig. 7, the *g*-values and the linewidths were extracted by fitting the spectrum to a derivative of Lorentzian profiles. The results are plotted in Figs. 7B, 7C, 7B' and 7C'. For both directions, at temperatures above 70 K, that is, $T > J$, the linewidth increases slightly with increasing temperature while the *g*-factor remains constant. At temperatures between 70 and 5.2 K, both the linewidth and the *g*-value increase rapidly upon cooling and then show a sharp kink at 5.2 K. This feature is due to enhanced short-range order correlations with a consecutive development of critical 3D correlations. As T approaches T_N, the temperature dependence of the linewidth is given by $\Delta H \propto (T-T_N)^{-p}$ where p is the critical exponent related to the anisotropy and the dimensionality of the spin system. The studied compound is described with p = 0.57(4) and 0.54(4) for g_z and g_x directions, respectively. These values are close to the reported value of p = 0.5 for the 1D case, confirming a low-dimensional character of the ESR line.[36]

A decrease in the g-value (equivalently, an increase in the resonance field) means the development of an internal magnetic field parallel to the applied field, that is, a ferromagnetic component. This is compatible with an antiferromagnetic chain with ferromagnetic interchain interactions and gives a support for our theoretical calculation.

In a magnetically ordered state the linewidth of an antiferromagnetic resonance is determined by four magnon scattering processes and an occupation number of magnon excitations. Its temperature dependence can be phenomenologically described with a power law $\Delta H \propto T^n$ with n = 3.2 when $B \parallel g_z$ (Fig. 7C). This is slightly smaller than the T^4 dependence expected for a conventional antiferromagnet.[37] This might be associated with a low-dimensional nature of the underlying spin system. For the case of $B \parallel g_x$ (Fig. 7A'), a splitting of EPR peak is observed, which is ascribed to a second branch of antiferromagnetic resonances. For two sublattice systems, in principle, two antiferromagnetic resonances are possible.

For spin chain compounds $LiCuVO_4$ and $KCuF_3$ in the high-temperature paramagnetic region, the temperature dependence of the linewidth is described by the empirical exponential law $\Delta H \propto \exp[-C_1/(C_2+T)]$ with fitting parameters C_1 and C_2.[38] Contrarily, the increase in the line-width is marginal in the case of DMACuF. This suggests that the line broadening mechanism in DMACuF is different from that in $LiCuVO_4$ and $KCuF_3$, possibly due to negligible anisotropic exchange interactions for the former.

4.4 Dielectric Anomalies

As shown in Fig. 8, we observe no appreciable field dependence of ε' by applying an external field up to 7 T. This implies that there is no substantial field induced change of magnetization. In addition, we find no evidence for a spontaneous polarization. In contrast to other DMAMFs, the dielectric anomalies of DMACuF at T_N are due to a second-order effect, possibly mediated by AFM fluctuation. The overall temperature dependence can be explained by Lyddane-Sachs-Teller relation between the dielectric constant and the phonon modes, $\varepsilon_o = (\omega_L^2/\omega_T^2)\varepsilon_\infty$, where ω_L (ω_T) is the long-wavelength longitudinal (transverse optical (TO)) phonon frequency and ε_o (ε_∞) is the dielectric constant at zero (infinite) frequency.[39] The TO modes undergo usually a softening through spin-lattice coupling. In this picture, the minimum of ε' for temperatures above T_N is correlated to a decrease in the phonon frequency. On the other hand, the kink of ε' at T_N can be a result of exchange striction or a spin fluctuation effect originated from the bi-quadratic magnetoelectric term.[40] To understand the underlying mechanism of the magnetodielectric effect at the AFM transition, it is needed to investigate lattice constants and optical phonon modes as a function of temperature.

5. Concluding Remarks

In summary, our magnetic susceptibility measurements and density functional calculations reveal that DMACuF consists of S=1/2 Heisenberg antiferromagnetic chains running along the c-direction, with $J_{intra} \approx +77.4$ K. The interchain coupling is much weaker, with $J_{inter} \approx -2$ K, showing it to be a nearly ideal 1D antiferromagnet. This is a 3 D crystal structure in which 1 D magnetic behavior is made possible by the Jahn-Teller distortion of the d^9 Cu^{2+} ions. The heat capacity of DMACuF clearly shows a phase transition to a 3D antiferromagnetic state at 5.2 K,

and so does the temperature dependence of the *g*-values determined from HF-EPR measurements. The EPR linewidth exhibits a $T^{3.2}$ behavior, which is close to the T^4 dependence expected for a conventional antiferromagnet. For temperatures below 5.2 K DMACuF is predicted to adopt an A-type antiferromagnetic structure in which the magnetic unit cell is identical to the chemical unit cell. The dielectric measurements show a sharp anomaly in the dielectric constant at T_N, adding a novel characteristic to this MOF.

Acknowledgments

The National High Magnetic Field Laboratory is supported by NSF Cooperative Agreement No. DMR-0654118, and by the State of Florida. K.Y.C. acknowledges financial support from the Priority Research Center Program funded by the NRF of Korea Grant No. 2009-0093817. H.-J. Koo thanks for financial support from the Basic Science Research Program through the NRF of Korea funded by the Ministry of Education, Science and Technology (2010-0021042).

Figure captions

Figure 1. (a) Zoomed-in view of the crystal structure of DMACuF at 110 K. (b) The axially-elongated CuO_6 octahedron with the perspective view of its magnetic orbital in DMACuF. (c) Projection view of a single layer of DMACuF, where the red line represents the "intrachain" spin exchange path J_1, and the green and blue lines the "interchain" spin exchange paths J_2 and J_3, respectively. $J_1 >> |J_2| > J_3$. (d) 3D view of spin exchange paths in DMACuF.

Figure 2. Temperature dependence of the FC and ZFC magnetic susceptibilities measured for a single crystal of DMACuF with the magnetic field of 0.5 T applied along the g_z-axis of the crystal. The solid curve represents a fit to the Bonner-Fisher formula, and the dashed line a fit to a Curie-Weiss law to the ZFC data with Curie-Weiss temperature $\theta = -80.6$ K. The crystal has a size of ~ 1×1×0.5 mm (L×W×H) and the shape is shown in the inset of Fig. 6A.

Figure 3. Magnetization versus field measured at 1.8 K with magnetic field applied along the g_z-axis of the crystal. The inset: Magnetic susceptibility $\chi(H) = dM/dH$, obtained by a derivative of the magnetization. Dashed lines are a guide to the linear dependence of the magnetization. The arrows indicate the magnetization jump induced by a spin-flop transition. The same crystal was used as in Fig. 2.

Figure 4. (A) Heat capacity of a polycrystalline sample at 0 T as a function of temperature. Inset: C_P/T^2 versus temperature. The solid line represents T^3 dependence of C_P below the transition temperature. (B) Temperature dependence of heat capacity at different magnetic fields. Inset: Phase diagram extracted from main figure.

Figure 5. A typical EPR spectrum of a powder sample with its simulation at 108 GHz and 150 K. ~ 5 mg crystals were grinded, mixed with 100 mg KBr, and pressed into a pellet for the EPR measurements.

Figure 6. (A) Angular dependence of effective g-values of a single crystal in three orthogonal planes. The solid lines are theoretical fits with the conventional expression $g = \sqrt{g'^2 \cos^2\theta + g''^2 \sin^2\theta}$. (B) A scheme showing the relation between the three principal g-axes and the unit cell axes. The same crystal was used as in Fig 2.

Figure 7 (A) Temperature dependence of EPR spectrum of a single crystal at 240 GHz with magnetic field applied along the g_z-axis of the crystal. (B) and (C) Extracted g-value and linewidth as a function of temperature. (A'), (B') and (C') are for the case when magnetic field is applied along g_x-axis.

Figure 8. Dielectric constant as a function of temperature at different magnetic fields.

Figure 9. Ordered spin arrangements of (a) FM, (b) AF1, (c) AF2 and (d) AF3 states in DMACuF, where the gray and white circles represent spin up and down Cu^{2+} sites,

respectively. The numbers in parenthesis, from left to right, are the relative energies with respect to the AF1 state obtained from GGA+U calculations with U = 4, 5, 6, and 7 eV, respectively.

Figure 10. (A) Projection view of two coupled CuO_6 octahedrons in a 1D chain, showing the relative orientations of bonding. (B) A cartoon showing the relation between the principal *g*-vectors ($g_{\parallel}$ and $g_{\perp}$) of two neighbor Cu centers and the three effective *g*-values measured in Fig. 5. (C) A scheme showing the relation between the vectors.

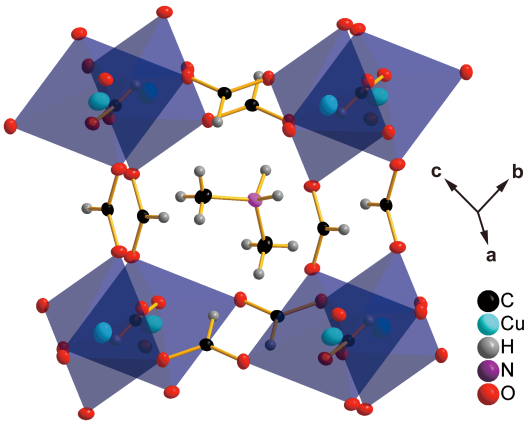

(a)

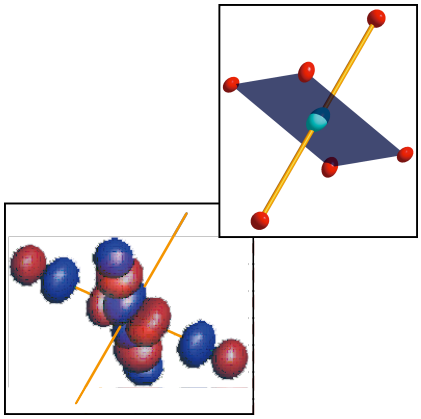

(b)

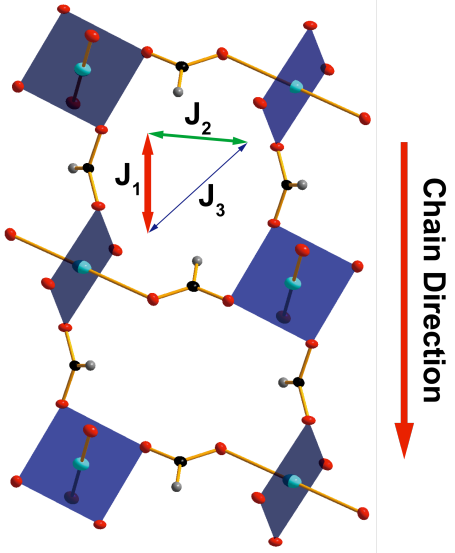

(c)

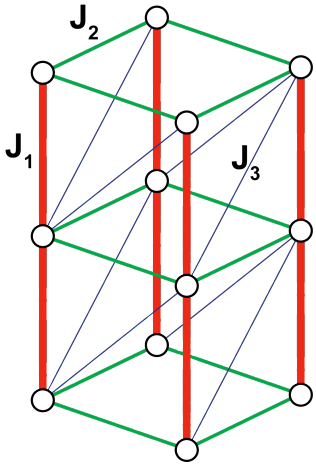

(d)

Figure 1.

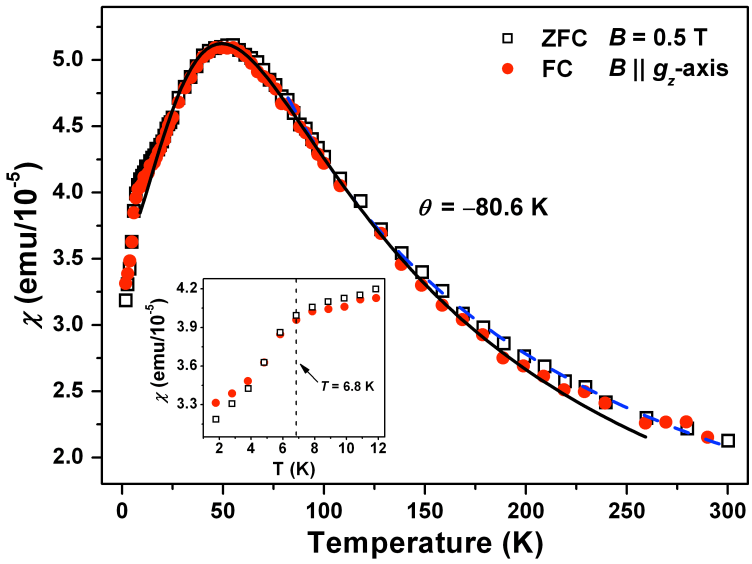

Figure 2.

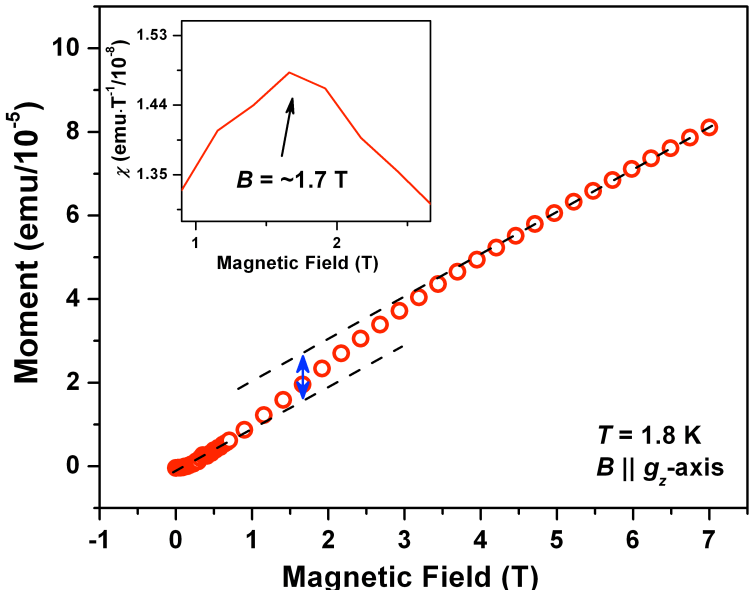

Figure 3.

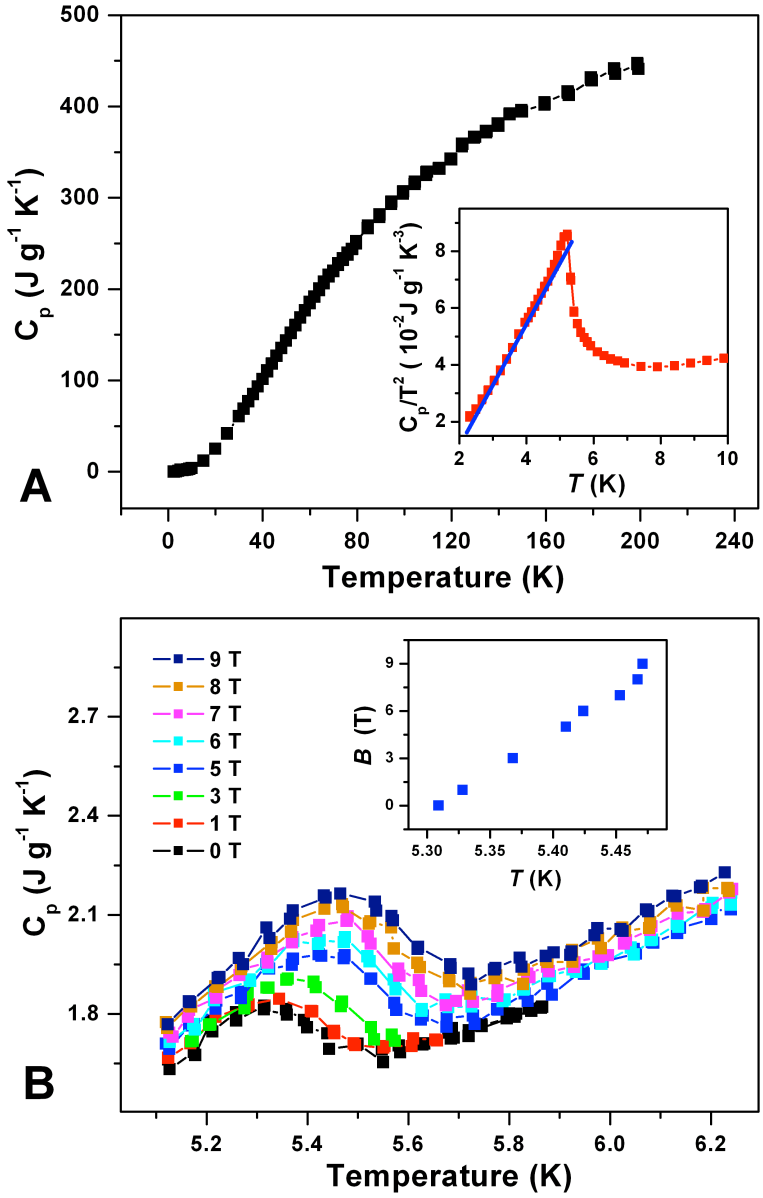
A
C_p (J g^{-1} K^{-1})
Temperature (K)
C_p/T^2 (10^{-2}J g^{-1} K^{-3})
T (K)
B
9 T
8 T
7 T
6 T
5 T
3 T
1 T
0 T
B (T)
T (K)
C_p (J g^{-1} K^{-1})
Temperature (K)

Figure 4.

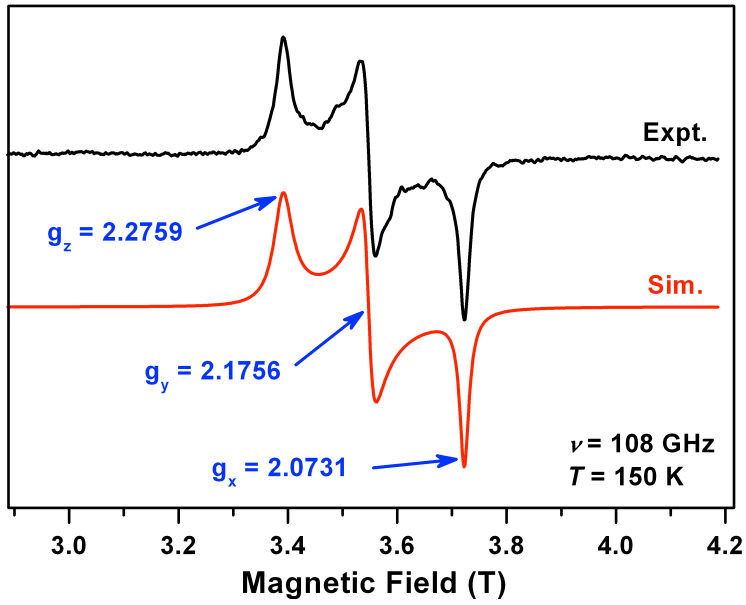
Expt.
Sim.
g_z = 2.2759
g_y = 2.1756
g_x = 2.0731
ν = 108 GHz
T = 150 K
3.0
3.2
3.4
3.6
3.8
4.0
4.2
Magnetic Field (T)

Figure 5.

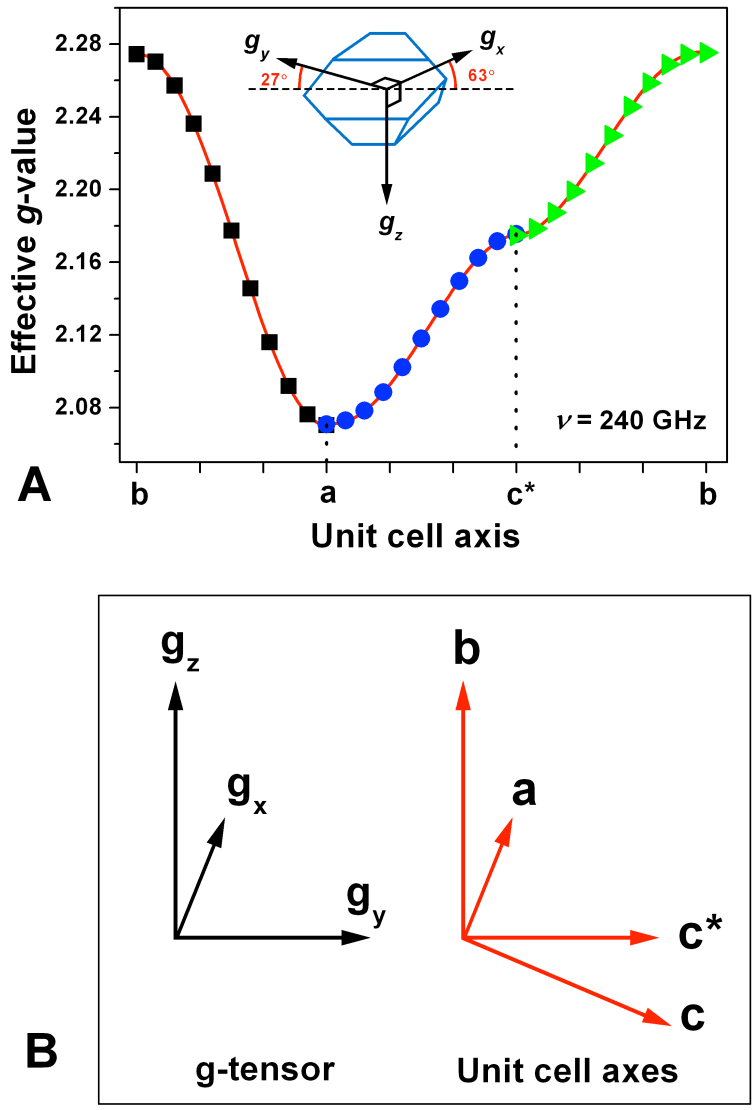
A
Effective g-value
2.28
2.24
2.20
2.16
2.12
2.08
g_y
g_x
27°
63°
g_z
ν = 240 GHz
b
a
c*
b
Unit cell axis
B
g_z
g_x
g_y
g-tensor
b
a
c*
c
Unit cell axes

Figure 6.

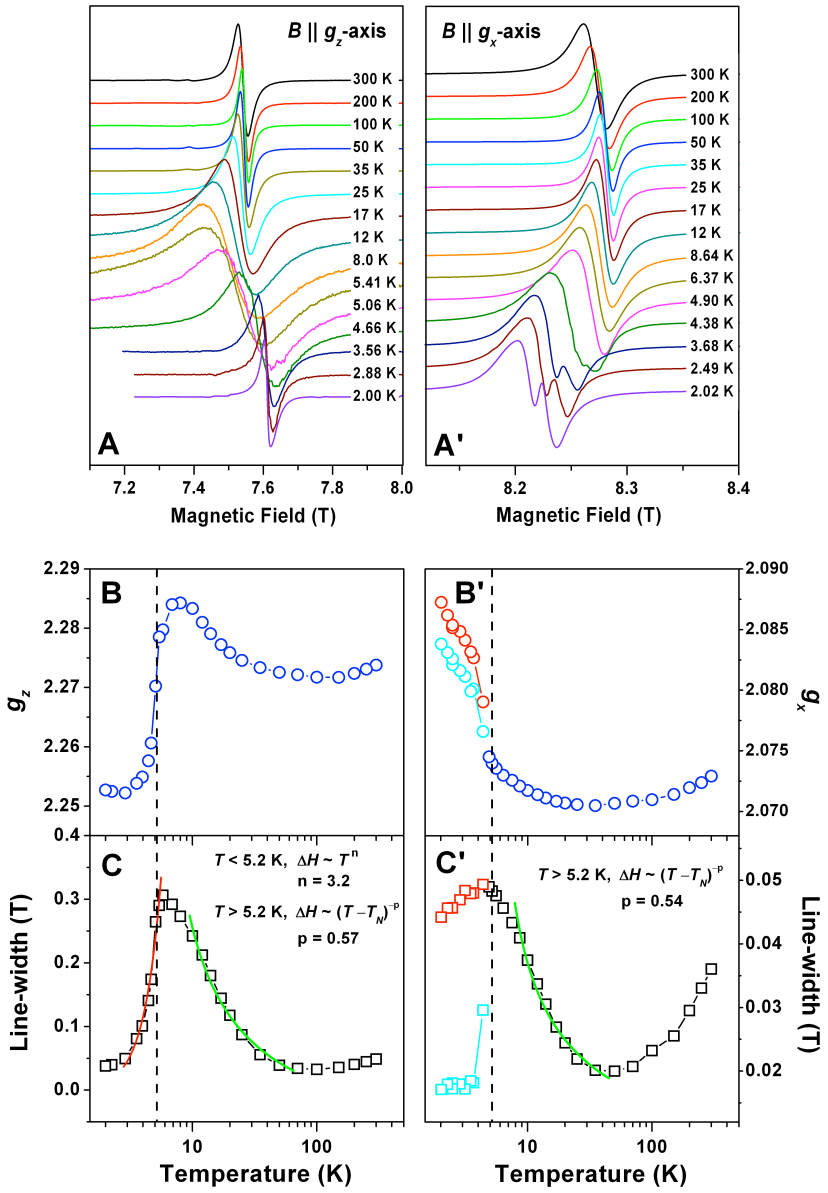
B || g_z-axis
300 K
200 K
100 K
50 K
35 K
25 K
17 K
12 K
8.0 K
5.41 K
5.06 K
4.66 K
3.56 K
2.88 K
2.00 K
A
7.2
7.4
7.6
7.8
8.0
Magnetic Field (T)
B || g_x-axis
300 K
200 K
100 K
50 K
35 K
25 K
17 K
12 K
8.64 K
6.37 K
4.90 K
4.38 K
3.68 K
2.49 K
2.02 K
A'
8.2
8.3
8.4
Magnetic Field (T)
B
B'
g_z
g_x
2.29
2.28
2.27
2.26
2.25
2.090
2.085
2.080
2.075
2.070
C
T < 5.2 K, ΔH ~ T^n
n = 3.2
T > 5.2 K, ΔH ~ (T −T_N)^-p
p = 0.57
C'
T > 5.2 K, ΔH ~ (T −T_N)^-p
p = 0.54
Line-width (T)
0.4
0.3
0.2
0.1
0.0
0.05
0.04
0.03
0.02
10
100
Temperature (K)
10
100
Temperature (K)

Figure 7.

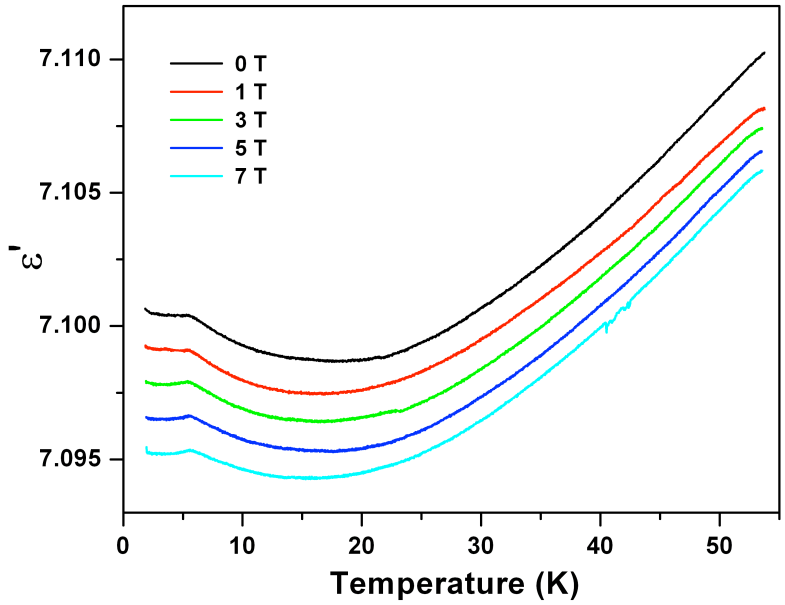

Figure 8.

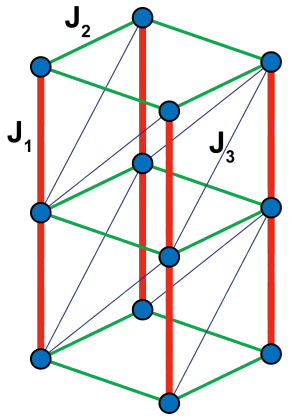

(a) FM (46, 38, 31, 25)

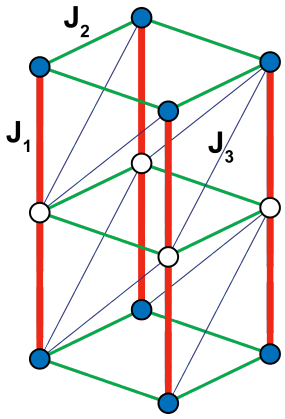

(b) AF1 (0, 0, 0, 0)

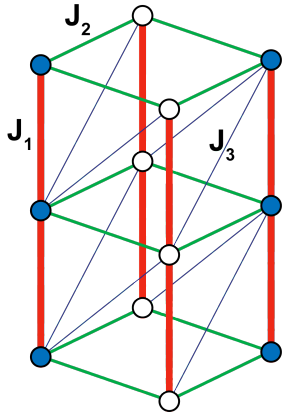

(c) AF2 (49, 40, 33, 26)

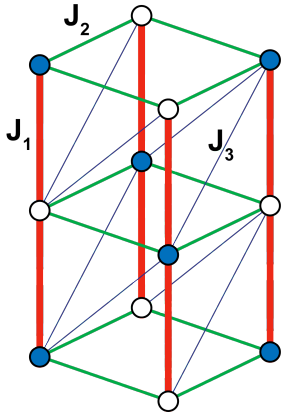

(d) AF3 (5.4, 4.0, 3.0, 2.2)

Figure 9.

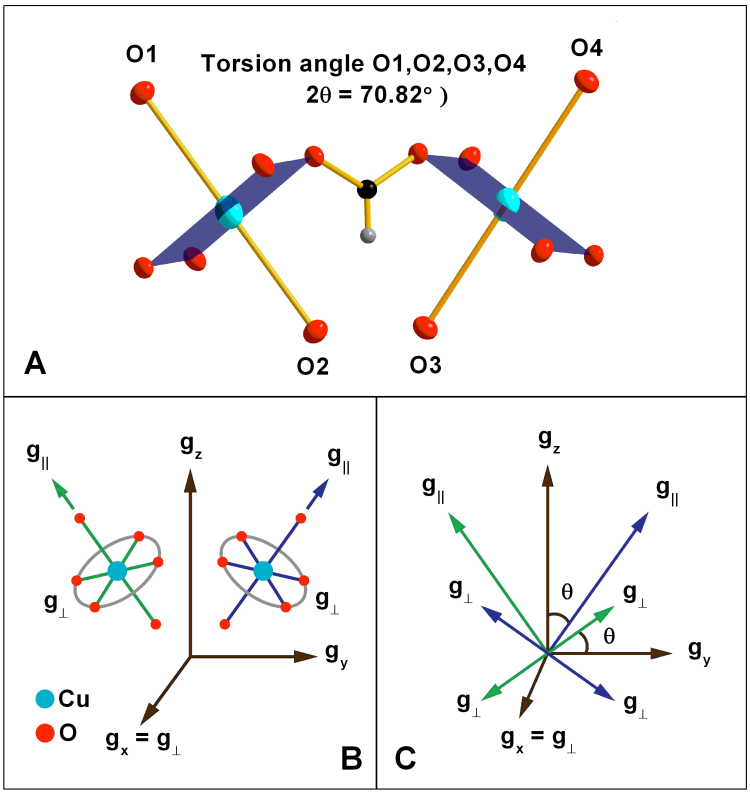

Figure 10.

Table 1. Values of the spin exchange parameters (in K) evaluated from GGA+U calculations

	U = 4 eV	U = 5 eV	U = 6 eV	U = 7 eV
J_1/k_B	258	214	176	143
J_2/k_B	-12	-8.8	-6.5	-4.9
J_3/k_B	3.5	2.7	2.0	1.5

References

[1] D. Farrusseng, S. Aguado, and C. Pinel, Angew. Chem., Int. Ed. **48**, 7502 (2009).

[2] P. M. Forster and A. K. Cheetham, Top. Catal. **24**, 79 (2003).

[3] G. Férey, Chem. Soc. Rev. **37**, 191 (2008).

[4] A. K. Cheetham, C. N. R. Rao, and R. K. Feller, Chem. Commun., 4780 (2006).

[5] A. K. Cheetham and C. N. R. Rao, Science **318**, 58 (2007).

[6] C. N. R. Rao, A. K. Cheetham, and A. Thirumurugan, J. Phys.: Condens. Matter **20**, 083202 (2008).

[7] P. Jain, N. S. Dalal, B. H. Toby, H. W. Kroto, and A. K. Cheetham, J. Am. Chem. Soc. **130**, 10450 (2008).

[8] P. Jain, V. Ramachandran, R. J. Clark, H. D. Zhou, B. H. Toby, N. S. Dalal, H. W. Kroto, and A. K. Cheetham, J. Am. Chem. Soc. **131**, 13625 (2009).

[9] T. Besara, P. Jain, N. S. Dalal, P. L. Kuhns, A. P. Reyes, H. W. Kroto, and A. K. Cheetham, Proc. Natl. Acad. Sci. U. S. A. **108**, 6828 (2011).

[10] A. Stroppa, P. Jain, P. Barone, M. Marsman, J. M. Perez-Mato, A. K. Cheetham, H. W. Kroto, and S. Picozzi, Angew. Chem. Int. Ed. **123**, 5969 (2011).

[11] Z. Wang, B. Zhang, T. Otsuka, K. Inoue, H. Kobayashi, and M. Kurmoo, Dalton Trans., 2209 (2004).

[12] X.-Y. Wang, L. Gan, S.-W. Zhang, and S. Gao, Inorg. Chem. **43**, 4615 (2004).

[13] M. Sánchez-Andújar, S. Presedo, S. Yáñez-Vilar, S. Castro-García, J. Shamir, and M. A. Señarís-Rodríguez, Inorg. Chem. **49**, 1510 (2010).

[14] E. Sletten and L. H. Jensen, Acta Crystallogr. **B29**, 1752 (1973).

[15] P. J. Baker, T. Lancaster, I. Franke, W. Hayes, S. J. Blundell, F. L. Pratt, P. Jain, Z. M. Wang, and M. Kurmoo, Phys. Rev. B **82**, 012407 (2010).

[16] M.-H. Whangbo, H.-J. Koo, and D. Dai, J. Solid State Chem. **176**, 417 (2003).

[17] H.-J. Koo and M.-H. Whangbo, Inorg. Chem. **47**, 4779 (2008).

[18] H.-J. Koo and M.-H. Whangbo, Inorg. Chem. **49**, 9253 (2010).

[19] G. W. Morley, L. C. Brunel, and J. van Tol, Rev. Sci. Instrum. **79**, 064703 (2008).

[20] J. van Tol, L. C. Brunel, and R. J. Wylde, Rev. Sci. Instrum. **76**, 074101 (2005).

[21] R. Samantaray, R. J. Clark, E. S. Choi, H. D. Zhou, and N. S. Dalal, J. Am. Chem. Soc. **133**, 3792 (2011).

[22] G. Kresse, Furthm, uuml, and J. ller, Phys. Rev. B **54**, 11169 (1996).

[23] G. Kresse and J. Hafner, Phys. Rev. B **47**, 558 (1993).

[24] G. Kresse and J. Furthmüller, Comput. Mater. Sci. **6**, 15 (1996).

[25] J. P. Perdew, K. Burke, and M. Ernzerhof, Phys. Rev. Lett. **77**, 3865 (1996).

[26] S. L. Dudarev, G. A. Botton, S. Y. Savrasov, C. J. Humphreys, and A. P. Sutton, Phys. Rev. B **57**, 1505 (1998).

[27] I. Tsukada, J. Takeya, T. Masuda, and K. Uchinokura, Phys. Rev. Lett. **87**, 127203 (2001).

[28] S. Stølen, T. Grande, and N. L. Allan, *Chemical Thermodynamics of Materials* (John Wiley & Sons, Ltd, Chichester, 2004).

[29] D. C. Johnston, et al., Phys. Rev. B **61**, 9558 (2000).

[30] Calculations were performed using EPRCalc developed by JvT.

[31] J. C. Bonner and M. E. Fisher, Phys. Rev. **135**, A640 (1964).
[32] H. J. Schulz, Phys. Rev. Lett. **77**, 2790 (1996).
[33] D. D. Dai and M. H. Whangbo, J. Chem. Phys. **114**, 2887 (2001).
[34] D. D. Dai and M. H. Whangbo, J. Chem. Phys. **118**, 29 (2003).
[35] E. O. Wollan and W. C. Koehler, Phys. Rev. **100**, 545 (1955).
[36] Y. Ajiro, S.-i. Matsukawa, T. Yamada, and T. Haseda, J. Phys. Soc. Jpn. **39**, 259 (1975).
[37] J. P. Kotthaus and V. Jaccarino, Phys. Lett. A **42**, 361 (1973).
[38] R. M. Eremina, M. V. Eremin, V. N. Glazkov, H. A. Krug von Nidda, and A. Loidl, Phys. Rev. B **68**, 014417 (2003).
[39] M. S. Seehra and R. E. Helmick, J. Appl Phys. **55**, 2330 (1984).
[40] G. Lawes, T. Kimura, C. M. Varma, M. A. Subramanian, N. Rogado, R. J. Cava, and A. P. Ramirez, Prog. Solid State Chem. **37**, 40 (2009).